Available online at www.sciencedirect.com

ScienceDirect

Catalysis Today 120 (2007) 78–89

CATALYSIS TODAY

www.elsevier.com/locate/cattod

Autothermal reforming of methanol: Experiments and modeling

James R. Lattner, Michael P. Harold *

Chemical Engineering Department, University of Houston, Houston, TX 77204-4004, USA

Abstract

A bench-scale fixed-bed reactor for the autothermal reforming (ATR) of methanol under near-adiabatic conditions was constructed to experimentally demonstrate the conversion of methanol to hydrogen over a copper-based catalyst. Axial distribution of air through multiple porous ceramic membranes was employed to limit the peak temperature within the catalyst bed, which is critical for the stability of copper-based catalysts. Methanol conversion, product selectivities, and temperatures were measured at discrete axial positions as a function of H_2O:C ratios, feed temperatures, pressures, and two different air distributor designs. The effect of space velocity was implicitly studied via the axial composition profile measurements while the O_2:C ratio was adjusted to achieve an overall methanol conversion exceeding 90%. The use of a copper-based catalyst with distributed air injection resulted in low CO effluent concentration of ca. 1.3% at a feed temperature of 200 °C, H_2O:C ratio of 1.0, O_2:C ratio of 0.11, and total pressure between 2 and 5 bar. Distributed air injection limits the peak bed temperature to 280 °C while injection of air over a narrow front results in a peak temperature of ca. 575 °C. The CO composition was found to be primarily a function of temperature and H_2O:C ratio, with CO yield minimized at low temperature and high H_2O:C. The system was simulated using an adiabatic 1D reactor model comprising kinetic rate expressions of Peppley et al. [B.A. Peppley, J.C. Amphlett, L.M. Kearns, R.F. Mann, Appl. Catal. A: Gen. 179 (1999) 31–49]. Very good agreement between data and model was achieved by assuming the oxidation reaction to be instantaneous (limited by oxygen supply). The results support a phenomenological view that the exothermic oxidation reactions occur in a narrow zone in close proximity to the porous membranes, leaving the bulk of the catalyst between membrane tubes in the reduced state and therefore active for conducting the endothermic reforming reactions.

Keywords: Autothermal reforming; Copper-based catalyst; Oxidation reaction

1. Introduction

Methanol is frequently considered as an attractive fuel for conversion to hydrogen for use in proton exchange membrane (PEM) fuel cells. It is produced from relatively abundant natural gas, and can be reformed to hydrogen at relatively mild conditions of ca. 250 °C. It can therefore be considered a transportable form of natural gas/hydrogen. With the proper choice of catalyst, an additional advantage of methanol is the production of a hydrogen product with a relatively low CO content. In conventional steam reforming (SR) of hydrocarbons, requisite heat to drive the endothermic chemistry is transferred from an external source to the reaction zone across a heat transfer boundary. The typical configuration is a multi-tubular reactor in which the generated heat of a combustion reaction is transferred through the tube walls. In the autothermal reforming (ATR) of hydrocarbons, air is fed with the hydrocarbon and water and the resulting oxidation reactions occur concurrently with the reforming. This can make for a simpler and more compact reactor design, comprising a fixed-bed of catalyst without any heat transfer components. The focus of the present work is the design, operation, analysis and modeling of a bench-scale adiabatic ATR reactor for the reforming of methanol to a hydrogen-containing product stream with low CO content.

A disadvantage of methanol as a fuel for hydrogen generation is a lack of infrastructure for its distribution. Hydrocarbons such as gasoline and diesel are readily available and the autothermal reforming of these fuels has been studied [1–5]. Hydrocarbon fuels require much higher reforming temperatures and result in high CO yields. While an ATR reactor with hydrocarbon fuels may be compact, the accompanying water gas shift (WGS) reactor, which converts the excess CO to CO_2 and hydrogen, can be quite large [6,7]

The application of autothermal reforming of alcohols for hydrogen production has been investigated previously. In the late 1980's, Johnson–Matthey developed a compact reformer

---

* Corresponding author. Tel.: +1 713 743 4307; fax: +1 713 743 4323.
E-mail address: mharold@uh.edu (M.P. Harold).

0920-5861/$ – see front matter © 2006 Elsevier B.V. All rights reserved.
doi:10.1016/j.cattod.2006.07.005

Nomenclature

A_{cs}	cross sectional area of reactor based on inside diameter
A^{*}_{surf}	surface:volume ratio of membrane or heat transfer surface
C_{Sj}	concentration of surface sites
C^{o}_{p}	molar heat capacity of gas mixture
E_a	Activation energy
ΔH_j	heat of reaction for reaction j
J_i	molar flux of component i within a catalyst pellet
k_j	rate constant for reaction j
K_i	adsorption equilibrium constant for component i
$K_{eq,j}$	reaction equilibrium constant for reaction j, $K_{eq,j} = \exp(-\Delta G_j/RT)$
N_g	molar flux of total gas stream in the axial direction of the catalyst bed
N_i	molar flux of component i in the axial direction of the catalyst bed
p_i	partial pressure of component i
r'_j	molar rate of reaction j based on mass of catalyst
r'''_j	molar rate of reaction j based on volume of catalyst solid
R	gas constant = 8.314 J mol^{-1} K^{-1}
R_p	particle radius
S_g	surface area of catalyst
T	pseudo-homogeneous reaction temperature
U_o	overall heat transfer coefficient
z	axial dimension

Greek letters

η_j	effectiveness factor for reaction j
υ_{ij}	stoichiometric coefficient for component i in reaction j
θ_{cat}	fraction of reactor cross section containing catalyst
ρ_b	catalyst bulk density

Subscripts

i	component number
j	reaction number

for the autothermal reforming of methanol over a copper–silica catalyst which they called the "Hot Spot^{TM}" reactor [8]. They used point injection of the reactants in the middle of the catalyst bed, creating a local high temperature heat source that drove the endothermic reforming reactions in the remainder of the catalyst bed. Reitz et al. [9] studied oxidation and reforming reactions over $CuO/ZnO/Al_2O_3$ catalyst, and found the catalyst to be inactive for reforming when exposed to oxygen. After all oxygen is consumed, the catalyst was reduced by methanol and became active for reforming.

Stability of Cu-based catalysts is a problem at temperatures above ca. 300 °C [10,11]. An improvement in both stability and activity has been found with quaternary catalyst compositions of $CuO/ZnO/ZrO_2/Al_2O_3$ [12–14]. Group VIII metals, and in particular Pd supported on ZnO, have been found to be active for steam and autothermal reforming of methanol [10,15–17]. These noble metal catalysts are much more stable than Cu-based catalysts, although not as selective for hydrogen formation. The differences can be attributed to different reaction mechanisms. For copper-based catalysts, Breen and Ross [12] propose a mechanism that involves the formation of a methyl formate intermediate, which decomposes to CO_2 as a primary product. CO formation, undesirable for PEM fuel cells, is attributed to the reverse water gas shift reaction. On Group VIII metals, direct methanol decomposition to CO and H_2 occurs [16]. CO is converted to CO_2 and H_2 by reaction with water in the forward WGS reaction. Both catalyst systems approach CO/CO_2 equilibrium with respect to the WGS reaction, albeit from different directions. Through kinetic control, the Cu-based systems are capable of producing CO levels well below equilibrium. At CO levels of about 1% or less, the need for a water gas shift reactor downstream of the reformer can be eliminated, and a preferential oxidation (PrOx) reactor or some other purification device can be used to further reduce the CO content of the reformate to the 10 ppm level required of the PEM fuel cell anode catalyst.

In our earlier work [18], we integrated a 1D adiabatic ATR reactor model with a process model of a PEM fuel cell system to simulate the production of electricity with methanol as the hydrogen source. This integrated model was used to test heat integration and process conditions for factors that influence fuel efficiency and reactor volume. A high fuel processor efficiency of 85% was achieved with a H_2O:C ratio of 0.8, a feed temperature of 200 °C, a pressure of 3 bar, and an O_2:C ratio of 0.13. This process model showed that higher H_2O:C ratios favor high methanol conversion and minimize CO formation, but a fuel efficiency penalty is encountered due to the higher water vaporization duty.

Our previous work utilized a kinetic reactor model developed based on available literature kinetic rate expressions. Separate rate expressions were utilized for the steam reforming and oxidation reactions. The steam reforming kinetics over $CuO/ZnO/Al_2O_3$ catalyst were derived by Peppley et al. [19] for the following reactions.

$$\text{Methanol steam reforming (SR)}: \quad \begin{array}{l} CH_3OH + H_2O \leftrightarrow CO_2 + 3H_2 \\ \Delta H^{o}_{f} = 49.4\,\text{kJ mol}^{-1} \end{array} \tag{1}$$

$$\text{Methanol decomposition (MD)}: \quad \begin{array}{l} CH_3OH \leftrightarrow CO + 2H_2 \\ \Delta H^{o}_{f} = 90.5\,\text{kJ mol}^{-1} \end{array} \tag{2}$$

$$\text{Water gas shift}: \quad \begin{array}{l} CO + H_2O \leftrightarrow CO_2 + H_2 \\ \Delta H^{o}_{f} = -41.1\,\text{kJ mol}^{-1} \end{array} \tag{3}$$

Reitz and coworkers found that copper catalysts, when exposed to oxygen, catalyze the complete combustion of methanol, and derived a kinetic rate expression over a CuO/

ZnO/Al_2O_3 catalyst [9]:

$$\text{Methanol combustion (MC)}: \quad CH_3OH + 1.5O_2 \leftrightarrow CO_2 + 2H_2O \quad \Delta H_f^o = -675.4\,\text{kJ mol}^{-1} \tag{4}$$

The scope of the present work is to demonstrate a compact autothermal reactor design that produces high hydrogen and low CO yields over a Cu-based catalyst. Critical to the selectivity and stability of the catalyst is the balancing of the exothermic oxidation and endothermic reforming reactions to avoid excessive temperatures. The design and operating conditions of the experimental reactor are selected based on the results of our previous work. Porous ceramic membranes are used to provide axial distribution of air. The design attempts to approach adiabatic operation to provide realistic temperature profiles for full-scale reactors. Provisions for measurement of the axial temperature and composition profiles are designed into the reactor. Experiments are performed under varied conditions of feed temperature, pressure, steam:carbon ratio, and with two different air distributor lengths. The effect of space velocity is implicitly studied via the detailed axial profile data. The results are discussed in terms of the variables that minimize CO yield. The benefits of adiabatic reactor temperature and composition profile measurements for gaining insight on reaction mechanisms and for the development of useful reactor models are also discussed.

2. Experimental set-up

A schematic diagram of the reactor is shown in Fig. 1 and an overall process flow diagram is shown in Fig. 2.

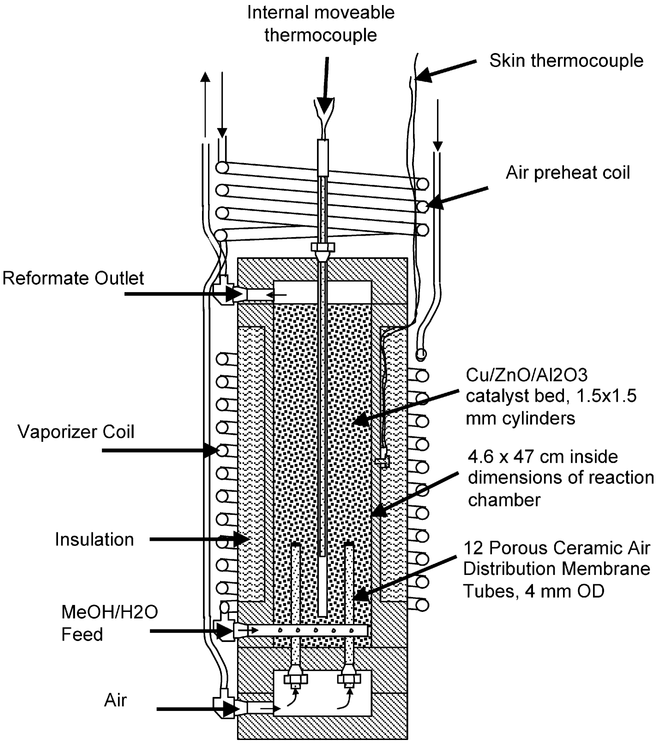

Fig. 1. Schematic diagram of adiabatic autothermal reforming reactor.

2.1. Reactor description

The reactor is a pressure vessel constructed of 316 stainless steel with inside dimensions of 4.6 cm I.D. × 47 cm long, capable of operating at pressures of 11 bar at 350 °C. The reactor is surrounded by a layer of insulation and is then wrapped with air preheat and feed vaporization coils. The entire assembly fits

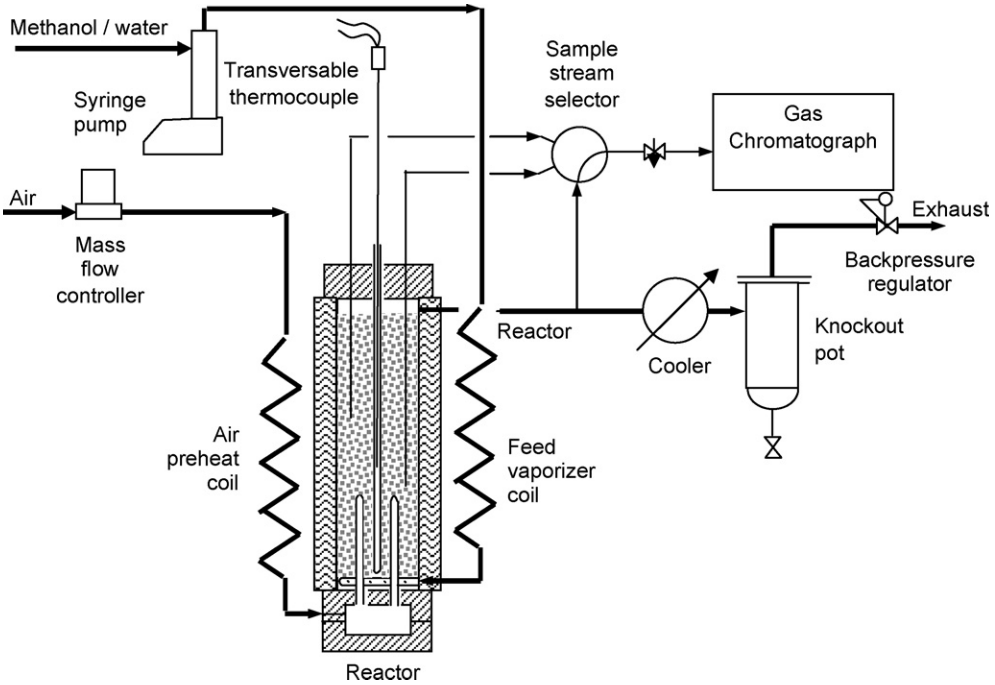

Fig. 2. Process flow diagram for the experimental unit.

inside a furnace with a 15 cm inside diameter. Thermocouples are attached to the outer skin of the reactor vessel under the insulation, and a single thermocouple transverses through a central internal thermowell (3.2 mm O.D.) using a stepper motor with a programmable step cycle.

The features that allow the reactor to operate at a close approach to adiabatic behavior are (i) a relatively large catalyst volume, such that heat transfer through the walls is small compared to the heat effects within the reactor; and (ii) a layer of insulation around the reactor and operation of the furnace so that there is a small temperature difference between the inside of the reactor and the surrounding furnace temperature.

The air is distributed axially through the bottom head of the reactor through 12 porous ceramic membrane tubes supplied by Ceparation®. The tubes are 4 mm O.D., 11.7 cm long and have a thin coating of γ-Al_2O_3 with nominal 800 nm pore diameter. The upper ends of the tubes are plugged with a proprietary glass composition that melts at 550–600 °C The pressure drop across the membrane at normal operating conditions is about 0.7 bar. This pressure drop is much higher than the pressure drop along the inside of the membrane tubes, ensuring uniform axial air distribution. The tubes are mounted into the bottom tubesheet with modified Valco® fittings using graphite ferrules. The methanol/steam vapor is introduced through a distributor in the bottom of the reactor. The distributor is a 9.5 mm O.D. tube with 8 holes of 0.8 mm diameter.

2.2. *Catalyst*

The reactor was loaded with 380 g of BASF V1765 catalyst, which is a $CuO/ZnO/Al_2O_3$ catalyst modified with ZrO_2. The catalyst,in the shape of cylinders with nominal dimensions 1.5 mm × 1.5 mm, was mixed with 1025 g of 3 mm diameter Pyrex® beads, such that the reactor volume contains 1/3 active catalyst by volume. Space velocities reported are based on 0.25 l of catalyst volume. The catalyst was reduced in a flowing stream of 2% hydrogen in nitrogen, starting at 90 °C and ramping to 225 °C over 3 h. The hydrogen concentration was then increased to 5% and held for 1 h.

2.3. *Feed and effluent system*

The methanol/water mixture was metered into the vaporizer coil with a pair of ISCO® syringe pumps (Model D500) to provide a continuous feed flow. House air dried with silica gel was fed to the reactor preheat coil using a Brooks® mass flow controller. The reactor effluent was cooled with water in a coiled jacketed tube exchanger. The condensate was collected in a knock-out pot and the cooled effluent gas stream was sent to a Mitey–Mite® backpressure regulator for pressure control.

2.4. *On-line gas analysis*

The reactor is fitted with nine internal sample probes for on-line gas analysis. These 1.6 mm O.D. tubes enter the top of the reactor through Valco® fittings and extend into the reactor at various axial positions. An additional probe samples the effluent gas stream. The 10 sample streams connect to a Valco® stream selector valve such that one stream at a time is directed to the gas chromatograph (Agilent® 6890) for analysis. All sample lines are electrically heated to prevent condensation. The sample flow rate to the gas chromatograph is controlled at 40–60 sccm. This flow rate represents less than 0.05% of the total reactor effluent rate, so that the sample withdrawal has a negligible effect on reactor performance. The gas analysis is carried out with a 30 m Haysep® DB column using helium as a carrier gas with a thermal conductivity detector. Quantification of H_2, N_2, CO, CO_2, H_2O and CH_3OH are obtained with this system. The overall cycle time for one analysis is about 30 min, such that about 5 h are required after the reactor is lined out to step through all 10 sample points. A mass balance around the reactor was performed using the nitrogen feed (via air) as an internal standard; mass balances within 2% were generally obtained. Further details about the analytical system will be provided elsewhere [20].

3. Reactor model

A one-dimensional reactor model was developed to simulate the performance of the adiabatic ATR reactor [18]. The axial temperature profile in an adiabatic reactor with competing exothermic and endothermic reactions is very sensitive to variations in the relative reaction rates. Comparisons are made between the measured and predicted axial temperature and composition profiles which will help to validate the kinetic model and to guide reactor design and analysis.

3.1. *One-dimensional reactor model*

The individual axial species molar fluxes (N_i) are determined by

$$\frac{dN_i}{dz} = \theta_{cat}\rho_b \sum_j \upsilon_{ij} r'_j \eta_j, \quad i = 1\ldots7, \quad j = 1\ldots4 \tag{5}$$

where the subscript i refers to the species and j refers to the reaction number. The volume fraction of catalyst in the reactor cross-section is represented by θ_{cat}. This term accounts for the cross-sectional area taken up by the air distribution tubes and the inert glass beads. Formally, the effectiveness factor of reaction j, η_j, is a function of temperature and reacting species concentrations for reaction j (discussed in more detail below). The r_j term contains the kinetic rate expression for each of the reactions based on catalyst mass, and ρ_b is the bulk catalyst density (1300 kg m^{-3}).

The axial distribution of the air feed was handled in the discretized form of Eq. (5) by dividing the oxidation zone into discrete segments. Each segment is then discretized and solved numerically. Oxygen and nitrogen are added to the beginning of each segment,

$$N_i^k = N_i^{k-1} + \frac{q_i^k}{A_{cs}}, \quad i = O_2, N_2, \quad k = 1\ldots n \tag{6}$$

where the superscript k refers to the discrete oxidation segment number, q_i is the flow rate of O_2 or N_2 added to segment k, A_{cs} is the reactor cross-sectional area, and n is the number of oxidation zone segments. In our previous modeling work, the oxidation zone was divided into 10–12 segments. In the present work, a better fit of the data was found using 100 or more segments and an instantaneous oxidation reaction, discussed in more detail in Section 5.

The one-dimensional energy balance is given by

$$N_g C_p^o \frac{dT}{dz} = \theta_{cat}\rho_b \sum_j (-\Delta H_j) r'_j \eta_j + A^*_{surf} U_o (T_w - T) \qquad (7)$$

The first term on the right hand side accounts for the heat of reaction, and the second term allows the inclusion of heat transfer to the outer wall. The heat capacity, C_p^o and heats of reaction ΔH_j are both functions of temperature. U_o is the one-dimensional overall heat transfer coefficient, $A^*_{surf}$is the wall surface area per unit volume, and T_w is the reactor wall temperature. The feed condition for each segment within the oxidation zone is corrected for the change in temperature due to the air addition:

$$T^k = \frac{N_g^{k-1} C_p^{k-1} T^{k-1} + (q_{air}^k / A_{cs}) C_p^{air} T_{air}}{N_g^k C_p^k} \qquad (8)$$

Axial dispersion of mass and heat are not included in the present model.

3.2. Kinetic rate expressions

The comprehensive methanol steam reforming kinetic model developed by Peppley et al. [19] has been used in this study. The model includes rate expressions for the aforementioned MR, WGS, and MD reactions as follows:

Methanol steam reforming:

$CH_3OH + H_2O \leftrightarrow CO_2 + 3H_2$

$$r'_{SR} = \frac{k_{SR} K_{CH_3O} (p_{CH_3OH} - (p_{H_2}^3 p_{CO_2} / K_{SR} p_{H_2O})) C_{S1} C_{S1a} S_g}{(p_{H_2}^{0.5} + K_{CH_3O} p_{CH_3OH} + K_{HCOO} p_{CO_2} p_{H_2} + K_{OH} p_{H_2O})(1 + K_H^{0.5} p_{H_2}^{0.5})} \left[\frac{\text{mol}}{\text{kg}_{cat}\,\text{s}}\right] \qquad (9)$$

Methanol decomposition:

$CH_3OH \leftrightarrow CO + 2H_2$

$$r'_{MD} = \frac{k_{MD} K_{CH_3O(2)} (p_{CH_3OH} - (p_{H_2}^2 p_{CO} / K_{MD})) C_{S_2} C_{S_{2a}} S_g}{(p_{H_2}^{0.5} + K_{CH_3O(2)} p_{CH_3OH} + K_{OH(2)} p_{H_2O})(1 + K_{H(2)}^{0.5} p_{H_2}^{0.5})} \left[\frac{\text{mol}}{\text{kg}_{cat}\,\text{s}}\right] \qquad (10)$$

Water gas shift:

$CO + H_2O \leftrightarrow CO_2 + H_2$

$$r'_{WGS} = \frac{k_{WGS} K_{CH_3O} p_{H_2}^{0.5} (p_{CO} p_{H_2O} - (p_{H_2} p_{CO_2} / K_{WGS})) C_{S1}^2 S_g}{(p_{H_2}^{0.5} + K_{CH_3O} p_{CH_3OH} + K_{HCOO} p_{CO_2} p_{H_2} + K_{OH} p_{H_2O})^2} \left[\frac{\text{mol}}{\text{kg}_{cat}\,\text{s}}\right] \qquad (11)$$

Table 1
Parameters for kinetic rate expressions for methanol reforming, decomposition, water gas shift, and oxidation reactions (units are consistent with pressures in bar and overall rate in mol $\text{kg}_{cat}^{-1}\,\text{s}^{-1}$)

Parameter	Expression
S_g	$1.02 \times 10^5\ \text{m}^2\,\text{kg}^{-1}$
$C_{S1} = C_{S2}$	$7.5 \times 10^{-6}\ \text{mol m}^{-2}$
$C_{S1a} = C_{S2a}$	$1.5 \times 10^{-5}\ \text{mol m}^{-2}$
k_{SR}	$7.4 \times 10^{14} \exp\left(\frac{-102{,}800}{RT}\right)$
k_{WGS}	$5.9 \times 10^{13} \exp\left(\frac{-87{,}600}{RT}\right)$
K_{MD}	$3.8 \times 10^{20} \exp\left(\frac{-20{,}000}{RT}\right)$
K_{CH_3O}	$6.55 \times 10^{-3} \exp\left(\frac{-20{,}600}{RT}\right)$
k_{OH}	$4.74 \times 10^{-3} \exp\left(\frac{20{,}600}{RT}\right)$
K_H	$5.43 \times 10^{-6} \exp\left(\frac{50{,}000}{RT}\right)$
K_{HCOO}	$2.30 \times 10^{-9} \exp\left(\frac{-100{,}000}{RT}\right)$
$K_{CH_3O(2)}$	$36.9 \exp\left(\frac{20{,}000}{RT}\right)$
$K_{H(2)}$	$3.86 \times 10^{-3} \exp\left(\frac{50{,}000}{RT}\right)$
$K_{OH(2)}$	$36.9 \exp\left(\frac{20{,}000}{RT}\right)$
ρ_b	$1300\ \text{kg m}^{-3}$

The parameters for Eqs. (9)–(11) are given in Table 1. K_{SR}, K_{MD}, K_{WGS} are the equilibrium constants for the SR, MD, and WGS reactions. The reaction equilibrium constants were calculated as a function of temperature using the physical property data and procedures outlined by Reid et al. [21].

In our previous work, we modeled the oxidation using the kinetic expression developed by Reitz et al. [9]:

Methanol combustion:

$CH_3OH + 1.5O_2 \leftrightarrow CO_2 + 2H_2O$

$$r'''_{OX} = k_{OX} \frac{p_{CH_3OH}^{0.18} p_{O_2}^{0.18}}{p_{H_2O}^{0.14}} \left[\frac{\text{mol}}{\text{kg}_{cat}\,\text{s}}\right] \qquad (12)$$

This rate expression did not achieve an adequate match of the exotherm data from our present work; an improved model will be discussed later.

3.3. Catalyst effectiveness factors

The species fluxes within a spherical catalyst pellet are described by the differential mole balances

$$\frac{dJ_i}{dr} = -\frac{2}{r} J_i - \sum_k \upsilon_{ik} r'''_k\,, \quad i = 1 \ldots 7, \ k = 1 \ldots 4 \qquad (13)$$

where J_i is the molar flux of species i (J_i is used to represent radial fluxes within the catalyst pellet to avoid confusion with N_i, the axial fluxes within the reactor). The reaction rate term is a function of the species partial pressures, which are subject to gradients due to diffusive and viscous resistances. The internal composition gradients are functions of the species fluxes and can be described following the method of Jackson [22]

$$\frac{J_i}{D^{\mathrm{e}}_{k,i}} + \sum_{j,j\neq i} \frac{x_j J_i - x_i J_j}{D^{\mathrm{e}}_{ij}} = -\frac{P}{RT}\frac{\mathrm{d}x_i}{\mathrm{d}r} - \frac{x_i}{RT}\left(1+\frac{B_0 P}{\mu D^{\mathrm{e}}_{\mathrm{k},i}}\right)\frac{\mathrm{d}P}{\mathrm{d}r}, \quad i = 1\ldots7,\quad j = 1\ldots7 \qquad (14)$$

Typically, simplifying assumptions are made to Eq. (14) to allow for direct substitution of the species fluxes into Eq. (13). This is not necessary for a numerical solution. Eq. (14) can be rewritten in terms of the partial pressure gradients:

$$\frac{1}{RT}\frac{\mathrm{d}p_i}{\mathrm{d}r} = -\frac{N_i}{D^{\mathrm{e}}_{k,i}} - \sum_{j,j\neq i}\frac{x_j N_i - x_i N_j}{D^{\mathrm{e}}_{ij}} - \frac{x_i B_0 P}{D^{\mathrm{e}}_{\mathrm{k},i}\mu RT}\frac{\mathrm{d}P}{\mathrm{d}r}, \quad i = 1\ldots7,\quad j = 1\ldots7 \qquad (15)$$

Note that the three terms on the right hand side represent contributions to the partial pressure gradients due to Knudsen diffusion, bulk (Stefan–Maxwell) diffusion, and viscous flow (D'Arcy's law), respectively. With 7 species in the present problem, there are a total of 14 coupled ODEs represented by Eqs. (13) and (15). The boundary conditions are zero gradients at the center of the catalyst pellet and partial pressures equal to the bulk partial pressures at the catalyst surface, assuming negligible external mass transfer resistance. The system is solved by integrating from the center of the pellet with an ODE solver, and iterating with the shooting method until the surface boundary conditions are satisfied.

The catalyst effectiveness for each reaction can then be calculated by ratioing the volume-integrated reaction rate with the rate that would have been obtained in the absence of internal pellet gradients:

$$\eta_j = \frac{3}{R_{\mathrm{p}}^3}\frac{\int_0^{R_{\mathrm{p}}} r_j''' r^2\,\mathrm{d}r}{\left. r_j''' \right|_{r=R_{\mathrm{p}}}}, \quad j = 1\ldots3 \qquad (16)$$

The effectiveness factors have been calculated for the 1.5 mm particles at various temperatures and conversions of methanol. (*Note*: The actual pellets are cylinders of 1.5 mm diameter and 1.5 mm length so we assumed a spherical shape.) The effectiveness factors were found to be rather strong functions of temperature and weak functions of theconversion. (The exception is when the composition is close to equilibrium and the reaction rates approach zero, the effectiveness factors can approach ± infinity.) Fig. 3 shows the results of the numerical computations of effectiveness factors for reactions 1–3, and a simplified regression for an overall effectiveness factor as a function of temperature. The effectiveness factor for the MD reaction is higher than SR or WGS, indicating that it has a slower rate. The regressed empirical expression is used for all three reactions in the 1D axial reactor model for computational efficiency. An effectiveness factor for the oxidation reaction was not applied because it was found to be rate-limited by oxygen supply (discussed in more detail below).

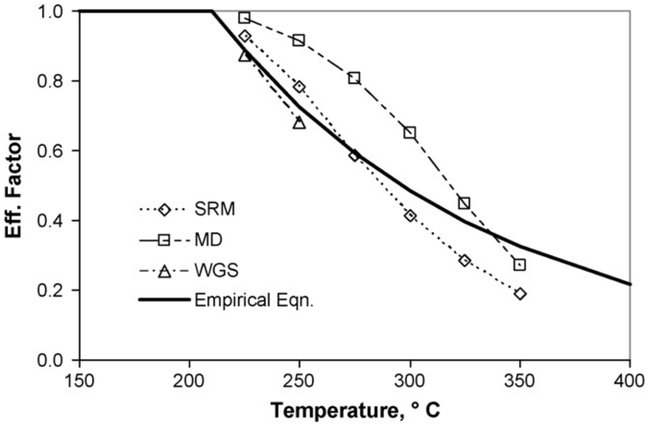

Fig. 3. Effectiveness factors for SR, WGS, and MD reactions in a 1.5 mm catalyst pellet with 300 Å average pore diameter.

4. Experimental results

Several experiments were conducted to measure the steady state axial temperature and composition profile in the reactor, and to determine the effects of operating variables on the methanol conversion and product distribution. The operating variables studied were feed temperature, H_2O:C ratio, total pressure, and air distribution membrane design. The effect of space velocity was implicitly studied because the axial composition and conversion profiles were measured. A narrow range of O_2:C ratios were utilized, as this was adjusted to maintain ca. 90–95% methanol conversion A total of 11 runs were carried out, the conditions for which are listed in Table 2. Table 2 also reports the measured conversion and effluent compositions.

Each run was started by first preheating the reactor and catalyst bed to about 200 °C, and then introducing the methanol/water feed mixture, followed shortly by introduction of the air feed. The furnace heat input was adjusted to control the target methanol/water feed temperature. The air feed preheat temperature was not controlled, as its preheat coil was in the same furnace zone as the feed vaporizer coil. The air feed temperature was generally higher than the methanol/steam feed temperature, but was constant for the duration of each run. Hydrogen production was generally observed within 1 min of feed introduction, however the system generally took about 1–2 h to completely line out with a steady state temperature and composition profiles.

Fig. 4 shows the axial temperature profile obtained for Run #9, which is typical of the other experiments conducted. The open squares represent the internal temperatures measured in the centerline thermowell. An elevated temperature of about 280 °C is encounteredin the oxidation zone, which is defined as the length over which the air distribution membrane tubes span. Beyond the oxidation zone, the temperature decreases monotonically due to the endothermic reforming reactions.

Fig. 5a–c show the axial conversion and species composition profiles for the same Run #9. The methanol conversion and hydrogen concentration are shown in Fig. 5a. The methanol conversion rises very sharply in the oxidation zone, followed by a slow increase in conversion and hydrogen concentration in the downstream reforming zone. The methanol conversion is

Table 2
(a) Experimental conditions for Runs 7–17 and (b) experimental results with predicted conversion and CO compositions for Runs 7–17

Run no.	GHSV	O_2:C	H_2O:C	Pressure (bar)	MeOH/H_2O feed temp	Air feed temp	Air distributor tube length (cm)	Cumulative run time on catalyst (h)
(a) Experimental conditions for Runs 7–17								
7	6779	0.113	0.99	1.70	220	300	11.7	7.0
8	8476	0.113	0.99	1.70	223	300	11.7	15.0
9	8476	0.113	0.99	4.09	223	300	11.7	22.0
10	8476	0.113	0.99	4.12	201	293	11.7	28.0
11	8519	0.111	0.80	1.91	219	298	11.7	33.0
12	8503	0.113	0.80	3.96	222	271	11.7	38.5
13	8519	0.111	0.80	4.98	203	303	11.7	43.3
14[a]	8787	0.126	0.80	1.88	163	283	11.7	51.3
15	9736	0.115	1.50	1.88	199	272	20.3	6
16	8503	0.113	0.99	3.96	222	271	20.3	11
17	8546	0.111	0.80	5.01	199	273	20.3	15

Run no.	Measured conversion (%)	Predicted conversion (%)	Measured H_2 (mol%)	Measured CO (mol%)	Predicted CO (mol%)	Measured CO_2 (%)	Measured CH_3OH (%)	Measured H_2O (%)	Measured N_2 (%)
(b) Experimental results with predicted conversion and CO compositions for Runs 7–17									
7	92.09	90.70	62.06	1.93	1.36	19.99	1.88	4.16	9.98
8	95.75	91.62	62.00	1.36	1.63	19.45	0.92	7.33	8.93
9	95.88	92.11	60.37	1.31	1.46	19.88	0.91	8.38	9.15
10	91.82	89.03	59.44	1.25	1.26	20.54	1.94	7.11	9.72
11	88.37	89.26	61.37	1.74	2.00	20.96	2.99	3.25	9.68
12	89.16	89.59	60.94	1.87	2.03	20.48	2.72	3.94	10.07
13	88.19	87.11	63.12	1.56	1.88	18.82	2.73	4.19	9.58
14[a]	92.89	83.30	58.59	2.80	3.20	17.48	4.23	6.84	10.77
15	97.46	87.60	54.73	0.39	0.56	19.28	0.51	16.29	8.80
16	95.47	89.15	62.43	1.43	0.95	19.32	0.99	6.36	9.47
17	89.47	85.73	62.07	1.24	1.10	19.88	2.49	5.20	9.13

[a] Data collected after upset, with peak temperature of 575 °C in bed. Catalyst changed after this run.

primarily to H_2 and CO_2 based on their respective axial profiles that reflect the ca. $H_2/CO_2 = 3$ stoichiometry of the reforming reaction (1). The corresponding H_2O and CH_3OH fractions decrease sharply. The trend for CO is more scattered than that of the other species, but appears to indicate a sharp initial production, followed by a slight decline in concentration.

During the experimental study a process upset occurred which resulted in an interruption in the methanol/water feed while air was still fed to the reactor (Run #14). This led to a momentary temperature excursion in the oxidation zone of the reactor. Upon return to normal operating conditions, a dramatically different temperature profile was obtained. Fig. 6a shows the steady state temperature profiles obtained prior to the upset, and Fig. 6b shows the steady state profile after the upset. Upon disassembly of the reactor, it was discovered that all of the end plugs in the air distribution membrane tubes had failed, resulting in the majority of the air being introduced at a single axial point about 10 cm into the reactor. The peak temperature achieved in this inadvertent test was about 575 °C. Although the catalyst was still active for reforming of methanol at this temperature, as evidenced by the endotherm following the oxidation zone in Fig. 6b, the activity was certainly declining rapidly due to sintering. Severe sintering and agglomeration of catalyst particles was visible in the catalyst bed upon disassembly.

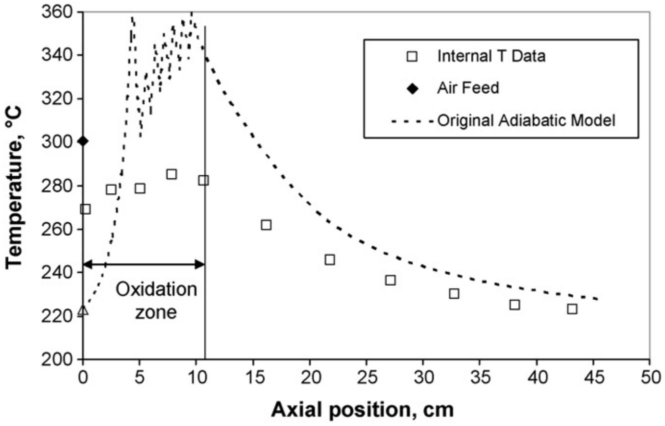

Fig. 4. Axial temperature profile (□) for the autothermal reforming of methanol in Run #9, GHSV = 8500 h^{-1}, O_2:C = 0.11, H_2O:C = 1.0, feed temperature = 222 °C. The dashed line represents the model prediction utilizing the oxidation kinetics of Reitz et al.

The length of the air distribution tubes was increased from 10.7 to 20.3 cm for Runs 15–17 in an attempt to further reduce the temperature rise in the oxidation zone while maintaining the same air feed rate. Runs 9 and 16 were run at identical conditions, as were Runs 13 and 17, with the only difference being the length of the air distribution tubes. Fig. 7 shows the axial temperature profile data for Runs 13 and 17. The peak temperatures in both of these runs were similar, about 279 °C. The peak temperatures were also similar in Runs 9 and 16. As shown in Table 2, there was a drop in CO composition from 1.6 to 1.2% from Run 13 to 17, although there was a slight increase in CO from Run 9 to 16, from 1.3 to 1.4%.

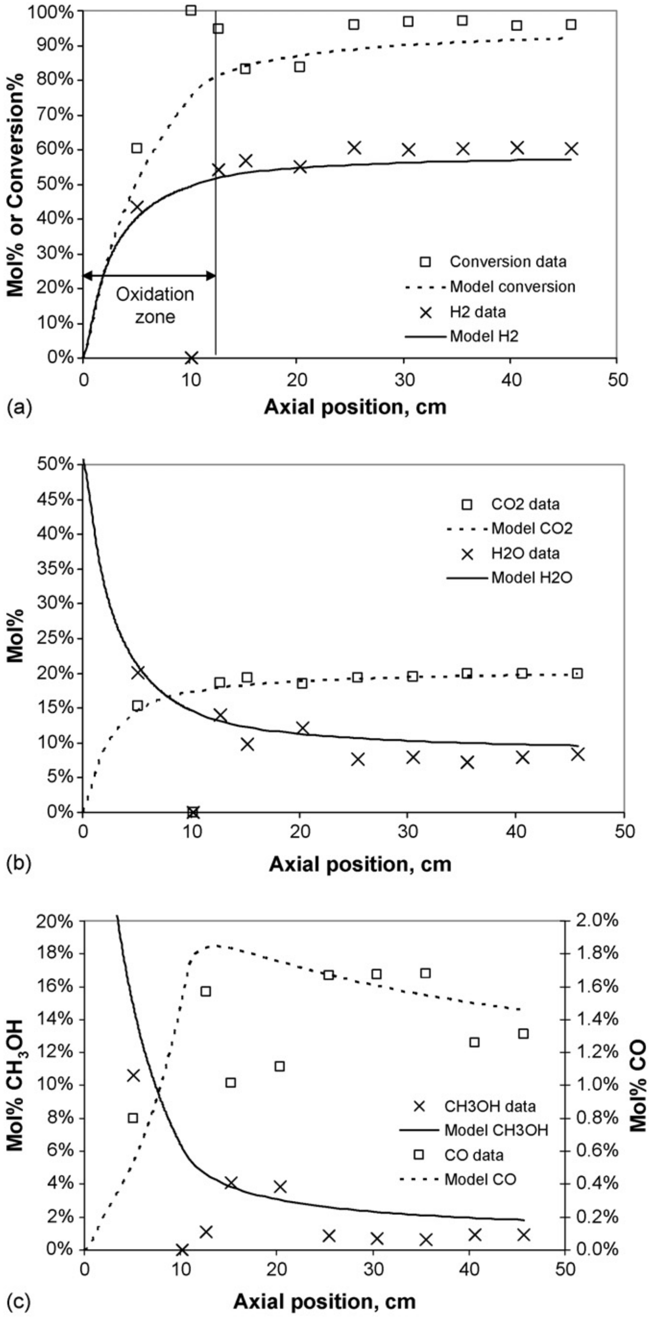

Fig. 5. Axial conversion and composition profiles for Run #9, along with model predictions: (a) conversion and hydrogen composition profile; (b) CO_2 and H_2O profiles; and (c) methanol and CO profiles.

It is believed that Cu-based catalysts are only active for the reforming chemistry in the reduced state. In Runs 7–14, the catalyst was pre-reduced in dilute hydrogen in a carefully controlled fashion. For distributed power applications, it would be desirable to simplify the catalyst reduction step. The fresh catalyst charge prior to Run 15 was reduced by feeding preheated methanol, steam and air to the reactor. The temperature rise in the reactor was difficult to control, as exothermic oxidation and reduction reactions were occurring in the bed. The procedure appears to have been effective at activating the catalyst for the reforming of methanol, as very similar results were obtained in Runs 16 and 17 as was found in Runs 9 and 13, respectively. A sample of reactor effluent taken within 5 min of the start of the methanol reduction procedure showed two unidentified peaks on the TCD. These peaks were absent in the next sample injection approximately 30 min later.

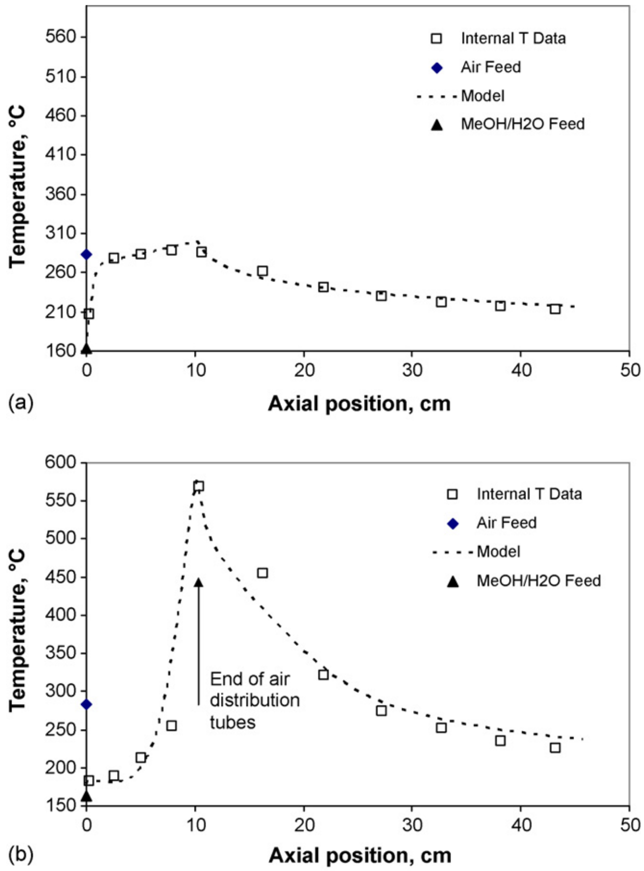

Fig. 6. Temperature profiles for Run #14, GHSV = 8800 h^{-1}, O_2:C = 0.13, H_2O:C = 0.8, feed temperature = 163 °C: (a) profile before upset with distributed air model prediction; and (b) profile after upset with model prediction assuming 90% of air injected at a single point.

The steam:carbon ratio has a significant effect on the CO content of the reformate. Run 11 was operated at an H_2O:C ratio

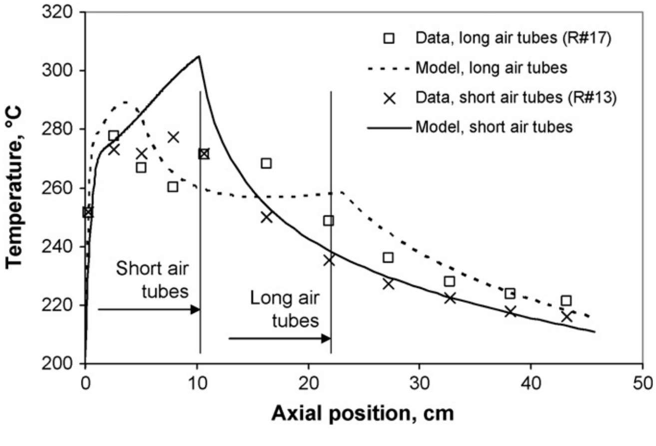

Fig. 7. Comparison of temperature profiles as a function of air distributor tube length. GHSV = 8500 h^{-1}, H_2O:C ratio = 0.8, O_2:C ratio = 0.11, feed temperature = 200 °C. Air membrane tube length = 11.7 cm for Run #13 and 20.3 cm for Run #17.

of 0.8 and Run 15 at a ratio of 1.5. The other operating variables were similar. The CO content at the low steam ratio was 1.7%, while the CO content at the high steam ratio was 0.4%.

The effect of pressure was tested with Runs 8 and 9. The pressure was increased from 1.7 to 4.1 bar, keeping other variables constant. The CO content and the methanol conversion changed very little, as shown in Table 2.

The oxygen:carbon ratio was adjusted in order to generate sufficient heat to result in a conversion of ca. 90–95%. Therefore, this variable could not be independently adjusted. The higher the steam:carbon ratio, the higher the O_2:C ratio required to achieve high conversion. This is because additional heat is needed to raise the temperature of the added diluent.

5. Analysis and discussion

We have shown that axial distribution of air accomplishes the objective of limiting the exotherm in an adiabatic reactor, maintaining a peak temperature below 300 °C. This allows operation in a regime where Cu-based catalysts are stable and selective to hydrogen with minimal CO formation. Stable operation has been demonstrated over a range of operating conditions.

We have carried out simulations of the experiments in order to elucidate the interactions between the oxidation and reforming reactions. The dashed line in Fig. 4 represents the original model prediction of the temperature profile. The saw tooth pattern is an artifact of the assumed discrete point (10 in total) addition of air. The model also predicts an induction zone wherein the temperature rise is negligible, followed by a sharp increase to a much higher temperature. These features are not evident in the data which shows a smoother temperature profile and an immediate increase in the temperature.

An improvement in the model prediction of the experimental data is obtained by increasing the rate of the oxidation reaction and by increasing the number of discrete air injection points. Rather than arbitrarily increasing the oxidation reaction rate constant, we tested the extreme case of instantaneous reaction (i.e. oxygen supply limited state) and found a good fit of the data.

The assumption of instantaneous oxidation reaction rate requires a modification to the feed condition Eqs. (6) and (8). The initial species fluxes and initial temperature are adjusted for the influence of the methanol combustion reaction at the beginning of each discrete oxidation zone segment.

$$\left\{ N_i^k = N_i^{k-1} + \frac{2}{3}\frac{q_{O_2}^{k}}{A_{cs}}\upsilon_{i,MC}, \quad i = O_2, CH_3OH, CO_2, H_2O, \quad k = 1 \ldots n \right\} \tag{17}$$

This equation changes the flux of each species involved in the MC reaction according to the stoichiometry of the MC reaction, $\upsilon_{i,MC}$. The 2/3 multiplier to the oxygen flow term puts the equation on a methanol basis. The nitrogen flux is also adjusted for the air addition as in Eq. (6).

The temperature at the start of each oxidation zone segment is affected by the addition of air, which is at a different temperature, as well as for the heat of the MC reaction.

$$T^k = \frac{N_g^{k-1}C_p^{k-1}T^{k-1} + q_{air}^k/A_{cs}C_p^{air}T_{air} + \Delta H_{MC}(2q_{O2}^k/3A_{cs})}{N_g^k C_p^k} \tag{18}$$

The first term in the numerator accounts for the heat capacity of the gas from the previous zone, the second term for the heat capacity of the air, and the third term for the heat of the methanol combustion reaction.

Fig. 8 shows the same data from Run #9 and model-predicted temperature profile assuming instantaneous oxidation of methanol. In assuming the oxidation rate is limited by the supply of oxygen the model predicts an immediate light-off of the reaction, even at feed temperatures as low as 163 °C. This model contains further improvements by (i) increasing the number of discrete injection points to 100, making air distribution essentially continuous; and (ii) by injecting 10% of the air ahead of the catalyst bed, representing the percentage of exposed air distribution tubing below the catalyst bed. As seen in Fig. 8, a good match of the profile in the oxidation zone is obtained.

Reitz et al. [9] showed that catalyst in the presence of oxygen was rather inactive for conducting the reforming reactions. In order to match the temperature profile data, we assumed that oxidation and reforming both occur in the oxidation zone of the reactor. If we were to assume that the catalyst in the oxidation zone were inactive for reforming, the exotherm would be in excess of 400 °C. This indicates that reforming and oxidation are both occurring because otherwise a much higher temperature rise would be observed. The axial composition profile also shows reforming activity in the oxidation zone, as evidenced by hydrogen production in the oxidation zone (Fig. 5a). What is likely is that the catalyst in close proximity to the air distribution tubes catalyzes the very fast oxidation of methanol, while the remaining catalyst further removed from the tubes where oxygen has been depleted remains in a reduced state and catalyzes the reforming reactions. A two-dimensional reactor model would be needed to fully capture this effect.

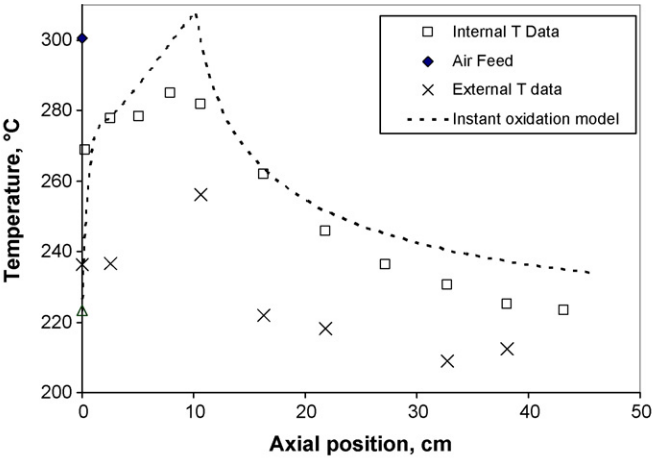

Fig. 8. Axial temperature profile for Run #9 and model prediction with the assumption of instantaneous oxidation kinetics. Data is the same as that shown in Fig. 4.

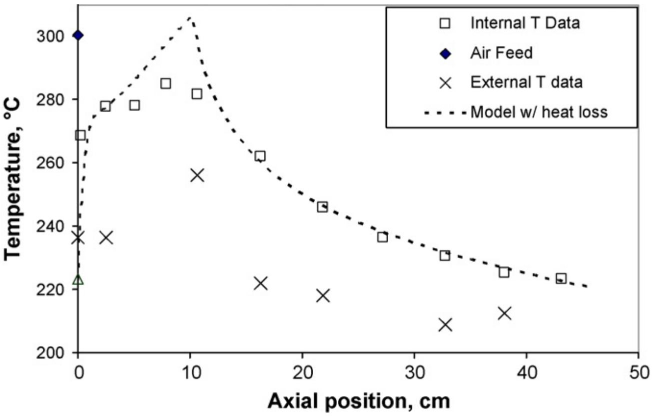

Fig. 9. Axial temperature profile for Run #9 and model prediction with instantaneous oxidation kinetics and heat loss through the wall.

While the reactor was designed to achieve adiabatic operation, the data indicate that some heat loss occurred. The reactor exit temperature predicted by the model is about 15 °C higher than the measured exit temperature (Fig. 8). Moreover, as indicated by the measured outer skin temperatures which are included in Fig. 5, the outer reactor skin temperature is about 20 °C cooler than the internal temperature along the length, despite the layer of insulation surrounding the reactor. It should be noted that the 15 °C temperature discrepancy represents less than 4% of the total exotherm that would occur from the oxidation reaction in the absence of endothermic reforming reactions of about 400 °C. This is evidence that a good approach to adiabatic behavior was achieved in the experimental apparatus. Nevertheless, these temperature discrepancies suggest that there is some heat loss through the reactor wall. A further improvement in the model prediction is obtained by utilizing a heat loss term (second term in Eq. (7)). A heat transfer coefficient of 75 J m^{-2} s^{-1} K^{-1} gives the model result shown in Fig. 9. The value of the heat transfer coefficient is reasonable considering that a commercial reforming furnace achieves a 1D heat transfer coefficient of 300–500 J m^{-2} s^{-1} K^{-1}, and it is expected that an insulated reactor will have a significantly lower coefficient.

A comparison of the model predictions of the reactant and product species profiles provides an even more sensitive test of the model. Fig. 5a–c compare the model predictions with experimental data for Run #9. Except for the data obtained from the second and third probes, the measurements are consistent with the model predictions. Fig. 5a shows the model prediction of the conversion and hydrogen composition axial profiles. The model predicts the trends very well, although the model slightly under-predicts the methanol conversion. This is likely due to the fact that the catalyst was fairly fresh during Run #9 and more active than aged catalyst. Fig. 5b shows the prediction of CO_2 and H_2O composition profiles. The prediction of CO_2 by the model is excellent; the slight discrepancy in water prediction is due to the same under-prediction of conversion. Fig. 5c shows the methanol and CO composition profile predictions. Although there is more scatter in the CO measurements compared with the other components, the model appears to capture the sharp increase in CO content in the oxidation zone, followed by a slow decrease in CO content as the extent of reforming reactions proceeds. We believe the reason for the high relative scatter of the CO data is due to the added measurement sensitivity at the low measured concentrations. At a given feed composition, the model predicts that CO yield is very sensitive to the reaction temperature. The initial sharp increase in CO content in the oxidation zone is caused by the higher reaction temperatures, increasing the rates of both MD and reverse WGS reactions. As the temperature drops in the remainder of the reactor, the catalyst is very selective to the steam reforming reaction, and the increase in molar flux due to hydrogen production dilutes the CO that was produced in the initial zone.

Note that the second and third sample results generally do not follow the expected trends for compositions. We believe this is due to the proximity of the sample probe to the air injection tubes. The first three sample probes are within the oxidation zone of the reactor. It is not known exactly where these probes were located relative to the surfaces of the air distribution tubes. It is possible that the second and third probes were very close or in direct contact with an air distribution tube. This would help to explain a local high conversion due to the locally high oxidation rate and would not be representative of the average radial composition. Oxygen was never detected in any of the samples collected, which is further evidence of the very fast nature of the oxidation reaction.

The dashed lines in Fig. 6a and b show the model prediction of the axial temperature profile data with and without good air distribution during Run #14. The model prediction of the temperature profile with good air distributors is shown in Fig. 6a. The temperature profile shown in Fig. 6b is after the upset that caused failure of the plugs in the ends of the air distribution tubes. The model prediction of this temperature profile was obtained by assuming that 90% of the air was introduced at the end of the air distribution tubes. The match with the measured data is remarkable, lending further validation to the usefulness of the model.

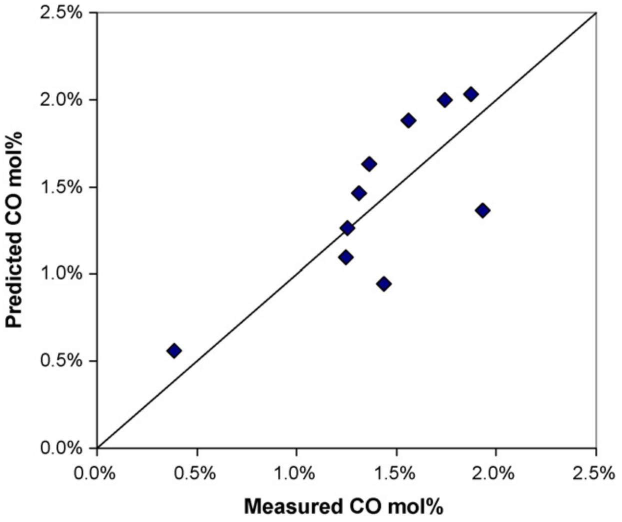

Fig. 10. Parity plot of the predicted vs. measured CO concentrations for all runs.

As can be seen from the data in Table 2, the measured conversion was generally higher than predicted by the model, but this gap closed as the catalyst aged, indicating some loss of catalyst activity over the 51 h duration of Runs 7–14. The catalyst was changed after Run 14 due to the temperature excursion described earlier.

The effect of air membrane tube length was modeled. The measured and predicted temperature profiles for Runs 13 and 17 are shown in Fig. 7. These runs were conducted at nearly identical feed temperature, pressure, and H_2O:C ratios, with the length of the air distribution membranes being the only variable. The model predicted that the peak temperature would be reduced with longer air distribution membranes, resulting in lower CO concentrations in the reformate. The data showed a reduction in CO, from 1.6% to 1.2% from Run 13 to Run 17, which is roughly in line with the model prediction (see Table 2). Runs 9 and 16 were also conducted at nearly identical conditions. Again, the model predicted a slight decrease in the CO concentration due to the lower peak temperatures (model profiles not shown). However, the data did not show such a reduction; the CO concentration increased slightly with the longer air membranes. We do not have a good explanation for the lack of a significant benefit for longer air distribution tubes. Perhaps there is debit for subjecting a greater portion of the catalyst bed to oxidizing conditions, which offset the benefits for a more distributed air feed.

The ability to predict CO selectivity and methanol conversion over a wide range of operating conditions is important for optimizing the design of a practical methanol fuel processor system. Figs. 10 and 11 show the predicted versus measured parity plots of CO composition and methanol conversion for the data presented in Table 2. The standard deviation in the CO prediction is within 0.2%, while the prediction of methanol conversion is within 3%. The activity of the catalyst appeared to decline somewhat over time, as the under-prediction of the conversion tended to decrease as the catalyst aged. The data gathered to-date does not allow development of a correlation for the activity decline due to thermal or oxidation-sintering of the catalyst.

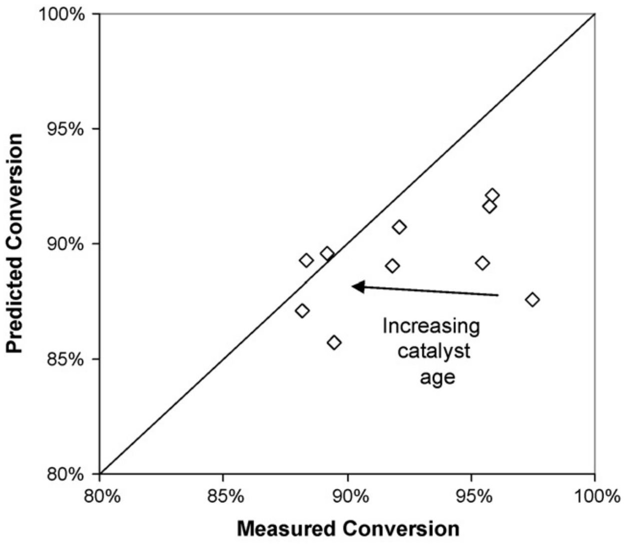

Fig. 11. Parity plot of the predicted vs. measure methanol conversion for all runs.

The main factors which affect CO selectivity are temperature and steam:carbon ratio. Low CO yield is favored with high steam:carbon ratios and low temperatures. Pressure has little effect on CO selectivity, an expected result based on the equimolar stoichiometry of the WGS reaction (3). Pressure is expected to suppress CO formation from the MD reaction (2), however,it appears this reaction rate is small at temperatures below ca. 300 C.

As shown in our previous work, increasing the steam:carbon ratio decreases the overall fuel processor efficiency due to the increased energy required to vaporize the water. The use of distributed air injection limits the peak temperature and flattens the temperature profile in an adiabatic reactor. To obtain the most compact reformer, the average temperature should be maximized to take advantage of faster reaction kinetics. The optimization of the design of an methanol ATR reactor is a balance between efficiency, size, and CO selectivity. An engineering reaction model such as the one developed here is important to allow such an optimization of design parameters to occur.

Good dynamic response is an important factor in the design of a reformer for distributed power applications. The experimental apparatus for the present study was not constructed to duplicate the dynamic response of an actual fuel processor. Rather, it was designed to gather steady state data under conditions approaching adiabatic. Clearly, schemes would need to be developed, such as (careful) pre-heating by methanol combustion or ohmic preheating, to achieve short startup times.

Some qualitative comments can be made regarding the reduction of fresh catalyst. It would be preferred to be able to start up a reformer without need to feed hydrogen for catalyst reduction. The use of preheated methanol, steam, and air was found to be effective at reducing the catalyst and making it active for conducting the reforming reactions. Reduction of the copper oxides is an exothermic reaction, and coupled with the exothermic MC reaction, control of the exotherm during startup required careful regulation of the air feed rate. A GC analysis of the reactor effluent during the startup revealed two unidentified peaks on the detector. These peaks quickly disappeared as the catalyst bed became completely reduced.

6. Conclusions

Copper-based catalysts for the reforming of methanol to hydrogen have the advantage of high activity and low selectivity to CO formation. The autothermal reforming of methanol over copper catalysts is feasible provided that the maximum bed temperature can be limited to about 300 °C. The axial distribution of air within the catalyst bed allows the exothermic oxidation reaction and the endothermic reforming reactions to occur in the same zone. Stable operation with autothermal reforming of methanol over a range of conditions was demonstrated with over 50 h of run time.

Conversion of methanol is favored by high steam:carbon ratio and high feed temperatures. The selectivity to CO is kept low at high steam:carbon ratio, low feed temperature, and with a moderated temperature rise in the oxidation zone: the temperature rise in the oxidation zone is reduced by increasing the length of the air distributors. The lowest measured CO concentration in the reformate was 0.4 mol% at a steam:carbon ratio of 1.5 and a feed temperature of 200 °C; the highest measurement was 1.7 mol% at a steam:carbon ratio of 0.8 and a feed temperature of 220 °C. The oxygen:carbon ratio must be adjusted to achieve the desired conversion level; higher air rates are required at high steam:carbon ratios and low feed temperatures. Experiments were conducted at pressures between 1.8 and 5 bar; no profound effect on CO yields or methanol conversion was observed as a function of pressure.

The use of an adiabatic laboratory reactor has proven useful for development and validation of an engineering kinetic model for autothermal reforming. The heat loss through the reactor walls is less than 4% of the total exotherm due to oxidation. The adiabatic temperature profile is very sensitive to small variations in the relative rates of exothermic and endothermic reactions. The experimental data is described well by a model that assumes the oxidation reactions are rate-limited by the supply of oxygen to the catalyst, and the reforming reactions follow the kinetic model developed by Peppley and coworkers. The only modification to the reforming kinetics was the inclusion of calculated catalyst effectiveness factors in the 1.5 mm catalyst cylinders.

Experiments by Reitz and coworkers show that catalyst exposed to oxygen is inactive for conducting reforming reactions. The present work clearly shows that catalyst in the oxidation zone of our adiabatic reactor is active for reforming of methanol. It is likely that the distribution of air, coupled with the high oxidation rates, restricts the amount of catalyst exposed to oxygen to the locality of the air distributors. This leaves the bulk of the catalyst between air distribution tubes in the reduced state, keeping it active for conducting the steam reforming reactions.

The distributed-feed membrane reactor affords an effective way of mitigating hot spot formation and of balancing coupled exothermic and endothermic reactions. Scalability should not be difficult with the distributed air addition. The main determinant of the total oxygen feed rate is the balancing of the energy generated by the exothermic oxidation with the endothermic energy requirements of the reforming chemistry. While it was not within the scope of the current study, the distributed air addition can be optimized in terms of the length of the oxidation section as well as the area per unit volume of the membranes. The results indicate that oxidation and reforming occurr in parallel in the front section of the reactor, even though the Cu catalyst is a reforming catalyst in its oxidized state. This implies that transverse gradients exist in the vicinity of the air supply membranes. A more detailed experimental and modeling study is underway to determine the effect of the number of membranes, membrane diameter, spacing, etc. on the overall reactor performance.

The distributed-feed membrane reactor model does a good job of predicting the main trends in the data with minimal parameter adjustments. A more detailed study of the effect of coupled oxidation and reforming on the activity of the catalyst would be needed to elucidate this important issue.

Finally, planned future work with this reactor system includes the addition of dense Pd alloy membranes within the reactor to test the concept of simultaneous reaction and separation.

Acknowledgements

This research was supported by the University of Houston, ExxonMobil Chemical Company, and the National Science Foundation (CTS-0521977).

References

[1] P.J. Berlowitz, C.P. Darnell, Proceedings of SAE Meeting, 2000, pp. 8–18.
[2] S. Ahmed, M. Krumpelt, Int. J. Hydrogen Energy 26 (2001) 291–301.
[3] A. Docter, A. Lamm, J. Power Sources 84 (1999) 184–200.
[4] M. Flytzani-Stephanopoulos, G.E. Voecks, Int. J. Hydrogen Energy 8 (1983) 539–548.
[5] L. Ma, D.L. Trimm, C. Jiang, Appl. Catal. A: Gen. 138 (1996) 275–283.
[6] L.F. Brown, Int. J. Hydrogen Energy 26 (2001) 381–397.
[7] J.R. Lattner, M.P. Harold, Int. J. Hydrogen Energy 29 (2004) 393–417.
[8] J.W. Jenkins, E. Shutt, Platinum Met. Rev. 33 (1989) 118–127.
[9] T.L. Reitz, S. Ahmed, M. Krumpelt, R. Kumar, H.H. Kung, J. Mol. Catal. A: Chem. 162 (2000) 275–285.
[10] S. Liu, K. Takahashi, K. Uematsu, M. Ayabe, Appl. Catal. A: Gen. 277 (2004) 265–270.
[11] Z. Wang, W. Wang, G. Lu, Int. J. Hydrogen Energy 28 (2003) 151–158.
[12] J.P. Breen, J.R.H. Ross, Catal. Today 51 (1999) 521–533.
[13] S. Velu, K. Suzuki, M.P. Kapoor, F. Ohashi, T. Osaki, Appl. Catal. A: Gen. 213 (2001) 47–63.
[14] S. Velu, K. Suzuki, M. Okazaki, M.P. Kapoor, T. Osaki, F. Ohashi, J. Catal. 194 (2000) 373–384.
[15] N. Iwasa, S. Kudo, H. Takahashi, S. Masuda, N. Takezawa, Catal. Lett. 19 (1993) 211–216.
[16] N. Takezawa, N. Iwasa, Catal. Today 36 (1997) 45–56.
[17] M. Lyubovsky, S. Roychoudhury, Appl. Catal. B: Environ. 54 (2004) 203–215.
[18] J.R. Lattner, M.P. Harold, Appl. Catal. B: Environ. 56 (2005) 149–169.
[19] B.A. Peppley, J.C. Amphlett, L.M. Kearns, R.F. Mann, Appl. Catal. A: Gen. 179 (1999) 31–49.
[20] J.R. Lattner, Ph.D. thesis, University of Houston, Houston, 2006.
[21] R.C. Reid, J.M. Prausnitz, B.E. Poling, The Properties of Gases and Liquids, fourth ed., McGraw-Hill, New York, 1987.
[22] R. Jackson, Transport in Porous Catalysts, Elsevier, Amsterdam, 1977.